Two different phytoplankton blooming mechanisms over the East China Sea during El-Niño decaying summers

Dong-Geon Lee[1,2], Ji-Hoon Oh[2], Jonghun Kam[1], Jong-Seong Kug*[2]

[1]Division of Environmental Science and Engineering, Pohang University of Science and Technology (POSTECH), Pohang, South Korea
[2]School of Earth and Environmental Sciences, Seoul National University, Seoul, South Korea

Correspondence to: Jong-Seong Kug (jskug@snu.ac.kr)

Abstract. During an El Niño-decaying summer, the East China Sea (ECS) has experienced anomalous phytoplankton blooming, but the understanding of associated generating mechanisms remains limited. Here, we analyzed observational (25 years) and long-term simulation data (1,000 years) to investigate the underlying mechanisms for the anomalous phytoplankton blooming in ECS. Results highlight two mechanisms associated with enhanced phytoplankton blooming in ECS during El Niño-decaying summers: inland runoff-driven and oceanic sub-surface upwelling-driven blooming mechanisms. Firstly, increased river discharge from the Yangtze River (YR) induces phytoplankton blooms. Secondly, wind-driven Ekman upwelling in ECS provides nutrients for phytoplankton from the sub-surface to the surface water layer. Rossby wave propagations from Western North Pacific Anti-Cyclone (WNPAC) cause a distinctive cyclonic atmospheric circulation over ECS that induces Ekman upwelling. The climate model simulation supports these two mechanisms, and thus our results suggest that both mechanisms contribute to the phytoplankton bloom concurrently.

1. Introduction

20

21   Numerous rivers, including The Yangtze River (YR), run into East China Sea (ECS). YR is the longest
22 river in Eurasia, contributing to a shallow continental shelf with high marine primary productivity (Liu et al., 2010,
23 2003; Tong et al., 2015; Zhai et al., 2023; Zhang, 1996; Zhao and Guo, 2011). Particularly, the Yellow Sea (YS)
24 and ECS, which belong to the East Asian Marginal Seas (EAMS), are known for being among the most productive
25 marine environments globally. Nutrients for phytoplankton growth are ample from the intrusion of nutrient-rich
26 Kuroshio intermediate water (Chen, 1996; Chen et al., 1995; Zhang et al., 2007), atmospheric deposition (Kim et
27 al., 2011; Zhang et al., 2010), and primarily riverine input from the YR (Huang et al., 2019; Wang et al., 2003).

28   Marine phytoplankton plays a role in the marine trophic chain (Danielsdottir et al., 2007), ocean carbon,
29 and biogeochemical cycles (Behrenfeld et al., 2006; Field et al., 1998). Chlorophyll-a (Chl-a) concentration is
30 widely used as a proxy for phytoplankton biomass and it has strength for handiness to measure from satellite
31 (Henson et al., 2010). The ECS region is surrounded by highly populated and developed nations with hundreds of
32 millions of people, which can have a profound impact on fisheries and marine ecosystems. Therefore,
33 understanding the spatio-temporal variability of phytoplankton in the ECS region associated with changes in river
34 discharge has great socio-economic importance, particularly in coastal communities.

35   ENSO plays a key role as a climate regulator for East Asia through its teleconnection. Western North
36 Pacific Anti-Cyclone (WNPAC) regulates the East Asian climate during ENSO events from the developing to
37 decaying phase (Kim and Kug, 2018; Li et al., 2017; Son et al., 2014; Wang et al., 2000). ENSO-induced changes
38 in the atmospheric and oceanic circulation alter physical properties in the ECS region, which can also affect the
39 marine ecosystems of the ECS region (Racault et al., 2017). During a decaying El-Niño summer season,
40 anomalous WNPAC transports warm and moist air from lower latitudes to East Asia, which increases regional
41 precipitation (Kwon et al., 2005; Li et al., 2021) and thus river discharge, carrying abundant nutrients into the
42 YECS region (Beardsley et al., 1985; Shi and Wang, 2012). This augmented river discharge impacts the coastal
43 ecosystems of eastern China and the western part of the Korean peninsula, potentially triggering anomalous
44 phytoplankton blooming (He et al., 2013; Park et al., 2015; Yamaguchi et al., 2012). The recent increasing trend
45 in surface chlorophyll-a in the ECS is correlated with nutrient concentrations without an increase in river discharge
46 (He et al., 2013). In addition, increased river discharge can cause anomalous phytoplankton blooming after strong
47 El Niño cases (Wu et al., 2023). These results suggest that there can be another process to induce the enhanced
48 phytoplankton blooming during El Niño decaying summer.

49   The WNPAC generated during the El Niño period not only increases riverine flows but also
50 accompanies anomalous cyclonic circulation over the EAMS region by the atmospheric Rossby wave propagation.
51 This induces Ekman upwelling (EKU) in the ECS region, transporting nutrients from the oceanic sub-surface to
52 the surface layer, and fostering anomalous phytoplankton blooming. An improved understanding of the additional
53 mechanism in conjunction with the existing one, will allow us to more accurately estimate the magnitude of
54 phytoplankton blooms in the ECS region during post El Niño summers. This could have implications for marine
55 resource management and fisheries in many neighboring countries.

56   Here, we propose another mechanism other than nutrient fluxes from the enhanced inland river

57   discharge. This study aims to understand the variability of phytoplankton concentrations in the ECS region during

58   the El Niño-decaying summers. We investigate both inland runoff-driven and oceanic sub-surface upwelling-

59   driven blooming mechanisms during El Niño decaying summers. The climate model long-term simulation and

60   observational data support these findings, highlighting the concurrent roles of both mechanisms in enhancing

61   phytoplankton blooming.

62   **2. Data and Methods**

63   **2.1. Reanalysis & Observation data**

64   We used the ocean colour satellite data from the European Space Agency Climate Change Initiative

65   Version (ESA-CCI) for chlorophyll-a data, serving as a proxy for phytoplankton biomass, covering 25-year

66   periods from 1998 to 2022 (Sathyendranath et al., 2019). El Niño events were identified using Extended

67   Reconstructed Sea Surface Temperature version 5 (ERSSTv5; Huang et al., 2017) Sea Surface Temperature (SST)

68   data from National Oceanic and Atmospheric Administration (NOAA), with anomalies greater than 1 standard

69   deviation during the winter season (December – January – February; DJF) index in the Nino3.4 (5°S-5°N / 170°

70   W-120°W) region. Furthermore, to examine atmospheric circulation such as wind, precipitation, and geopotential

71   height (GPH) changes, we analyzed the re-analysis data from the National Centers for Environmental Prediction

72   reanalysis version 2 / the National Center for Atmospheric Research (NCEP2 / NCAR; Kanamitsu et al., 2002).

73   Lastly, wind stress (τ) and wind stress curl (Curl$_{(\tau)}$; Kessler, 2006) are calculated followed as Eqs. (1)-(2) with

74   typical value for drag coefficient ($C_D = 0.0015$; Trenberth et al., 1990; Wyrtki and Meyers, 1976) and sea level

75   air density ($\rho_{air} = 1.225$ kg m^{-3}; Cavcar, 2000) with the square of zonal & meridional wind speed (V^2) from

76   NCEP2 re-analysis data.

77    $$\tau = \rho_{air} C_D V^2$$

78   (1)

79    $$\text{Curl}_{(\tau)} = \frac{\partial \tau_y}{\partial x} - \frac{\partial \tau_x}{\partial y} \tag{2}$$

80   **2.2. Model data**

81   We used the present climate-based (1990-year atmospheric CO_2 concentration level; 353 parts per

82   million (ppm)) long-term integrated simulations of the Geophysical Fluid Dynamic Laboratory (GFDL) - CM2.1

83   Earth System Model (ESM) fully coupled with the marine ecosystem model TOPAZv2 (Tracers of Ocean

84   Phytoplankton with Allometric Zooplankton Version 2; Dunne et al., 2013). The model incorporates various

85   external nutrient inputs such as atmospheric deposition, river nitrogen (N) input, and river inputs of dissolved

86   carbon, alkalinity, and lithogenic material; however not includes river phosphorus (P) inputs (Dunne et al., 2013).

87   The growth rate of phytoplankton is computed using a function of chlorophyll to carbon ratio and limited by

88   various factors in TOPAZ (Dunne et al., 2010). Nutrient limitation terms are determined by minimum limitation

89   values among micronutrients (Fe, PO_4, $Si(OH)_4$, $NO_3 + NH_4$).

90   Surface values in the model data were averaged to 30-meter depths, with spatial grid and temporal scale

91   set at 1° x 1° grid and monthly mean data, respectively. El Niño events were defined in the same methodology as

92   in the observation data. Statistical significance was calculated using the non-parametric bootstrap method, with

93   10,000 random samples replacing as many numbers of El Niño cases in observation and model results, respectively.

3. Results

3.1. Runoff-driven blooming mechanism - Insight from Observations

Figures 1a-b display the composite maps illustrating the spatial distribution of surface chlorophyll-a anomalies (SCHL) and precipitation anomalies during the El Niño decaying summer season (June-July-August; JJA). The pronounced anomalous SCHL blooming is observed from the Yangtze River Estuary (YRE) to the southern part of the Korean Peninsular. It has consistent patterns with the dispersal of strong river discharge from the YR (Park et al., 2015; Yamaguchi et al., 2012). In addition to the estuary of the YR region, there are also broad weak diagonal patterns of positive signal from northeastern Taiwan to the Korean Strait. This is in agreement with the relationship between Yangtze River Discharge (YRD) and SCHL in Yamaguchi et al, which has a lagged correlation from June to August and extends over a wide region from Jeju Island to the Korean Strait.
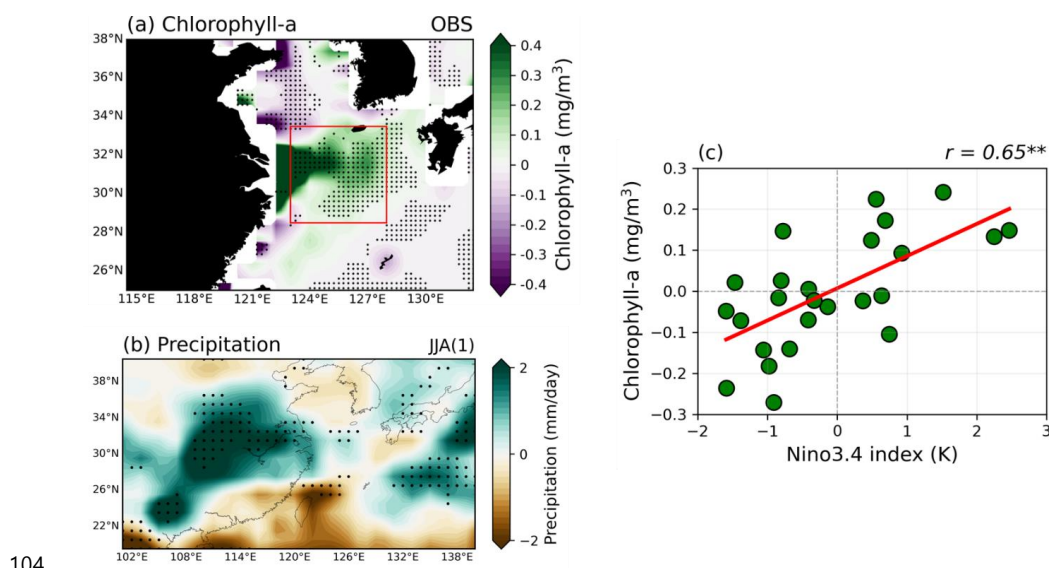
Figure 1. Composite maps exhibiting the 3-month average of **(a)** surface Chlorophyll-a (SCHL) anomalies, and **(b)** precipitation anomalies for El Niño decaying summer season (June-July-August; JJA) of all El Niño cases, using re-analysis and satellite data. **(c)** The relationship between the Niño3.4-DJF index which indicates the strength of El Niño mature phase and area-averaged SCHL anomalies over the research target area during the El Niño decaying summer season (Red box in Fig. 1a; 28.5°N-33.5°N / 122.5°E-128.5°E). All the black dots indicate where the responses are significant at the 95% confidence level by using the bootstrap method. ** marks indicate statistically significant correlation at the 99% confidence level.

This anomalous phytoplankton bloom during the boreal summer season of the following El Niño events has been explained by enhanced precipitation. In the El Nino years, the intensification of southwesterly winds by the Western North Pacific (WNP) high-pressure flow brings in warm and humid air from lower latitudes. This, in turn, leads to anomalous rainfall in the East Asian region (Figure 1b). Given the strong association between the variability of the YRD and precipitation, it is reasonable to anticipate that an increase in riverine input corresponds

118   to increased precipitation (Park et al., 2015). The lagged correlation between the Nino3.4 D(0)JF(1) index and the

119   SCHL anomalies in the ECS region (28.5°N-33.5°N, 123°E-128°E; target region indicated as red box in Fig. 1a)

120   during El-Niño decaying summers (JJA(1)) indicate significant positive relationship (r = 0.65**) at the 99%

121   confidence level (Figure 1c).

122   To comprehensively understand the mechanisms of phytoplankton blooms over the ECS during the

123   summer season after the ENSO mature phase, we first re-assessed the runoff-driven blooming mechanism,

124   commonly well-known from several previous studies. The robust positive signal in the precipitation anomalies is

125   centered in the southeastern part of China, where the YR flows. The intensified precipitation, consequently,

126   triggers an increase in river discharge, leading to anomalous SCHL blooming broadly over the YECS (Runoff-

127   driven blooming mechanism).

128

3.2. Runoff-driven blooming mechanism - Insight from Model

130   We further analyzed a long-term simulation using GFDL-CM2.1 ESM with a fully coupled

131   biogeochemical model to understand blooming mechanisms as well as the well-known runoff-driven blooming

132   mechanism. Notably, the GFDL-CM2.1 ESM does not simulate inputs of P from riverine inflows. In our target

133   area, the ECS region, climatologically, there is a strong influx of riverine runoff from the YR, which contains

134   excess Nitrate (N) concentrations (Kim et al., 2011; Moon et al., 2021; Wang et al., 2003). Under these marine

135   environmental characteristics, P is relatively constrained, and phytoplankton growth is controlled by changes in P

136   concentrations. In the oceans where P is the dominant factor regulating phytoplankton growth, especially in the

137   target region, the deficiency of P riverine inputs in the models may underestimate phytoplankton variability.

138   However, it affords us the advantage of exploring phytoplankton blooming mechanisms from another perspective,

139   not just a runoff-driven mechanism centered on the YRE region.

140   Prior to delving into further analyses, we verified that GFDL-CM2.1 ESM adequately simulates the

141   nutrient limitation in the target region (26.5°N-32.5°N, 122.5°E-128.5°E; target region in the model), with strong

142   P limitation observed in the YRE region and stronger N limitation appearing getting farther out (Figure 2). We

143   confirmed the nutrient limitation by separating the target region into the YRE and the extended YRE region (red

144   & blue box in Figs. 2e-f). In Figs. 2a-b, there is a relatively weak positive correlation (r = 0.25**) between surface

145   NO_3 and SCHL anomalies in the YRE region, while a higher significant positive correlation (r = 0.72**) in the

146   extended YRE region, indicating that N limitation begins to prevail. On the other hand, Figures 2c-d show a

147   significantly strong positive correlation (r = 0.88**) between surface PO_4 and SCHL anomalies in the YRE region

148   and no correlation (r = -0.03) over the extended YRE region. In particular, the partial correlation between the

149   surface PO_4 and SCHL anomalies after removing the effect of NO_3 in the YRE region is almost unchanged at

150   0.86**, while the opposite effect is even lower at 0.1**. The spatial distribution of partial correlations shows that

151   the effect of surface NO_3 on SCHL anomalies after removing the effect of surface PO_4 is stronger in the extended

152   YRE region. On the other hand, the effect of surface PO_4 on SCHL anomalies after removing the influence of

153   surface NO_3 is very strong not only in the YRE region but also over the YECS and Bohai Sea (Figures 2e-f). These

154   support the dominant P limitation in the YRE region, implying that the strong P limitation in the YRE region is

155   applied as well as the observations. These findings indicate the GFDL-CM2.1 ESM's ability to simulate the

156   relationship between phytoplankton growth and nutrients in the ECS region.
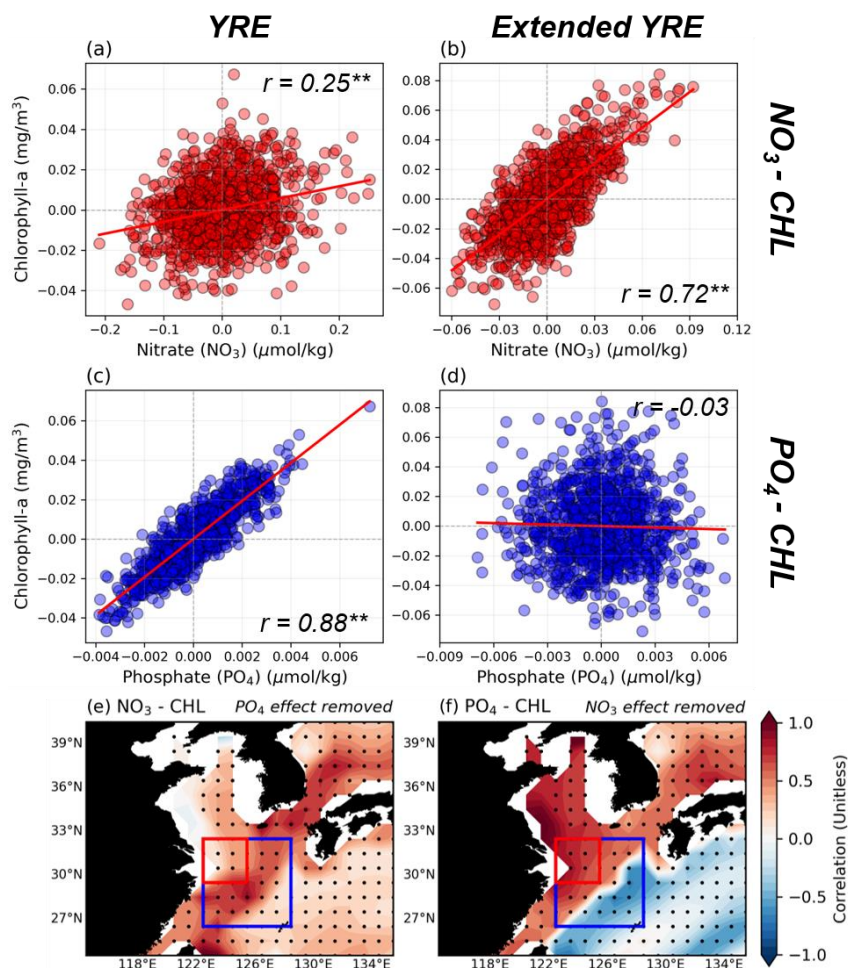
Figure 2. (a-d) The relationship between area-averaged surface nutrients and SCHL anomalies across the target
area. The upper panels (a-b) focus on the relationship between surface nitrate (NO_3) and SCHL anomalies in the
Yangtze River Estuary (YRE) [Left Panel; Fig. 2a] and extended YRE [Right Panel; Fig. 2b]. The lower panels
(c-d) indicate the relationship between surface phosphate (PO_4) and SCHL anomalies in YRE [Left Panel; Fig. 2c]
and extended YRE [Right Panel; Fig. 2d] within the ECS region respectively. **(e-f)** Partial correlation distribution
of the effect of surface NO_3 on SCHL anomalies after removing the effect of surface PO_4 and opposite case
respectively.

166   Figures 3a-c present the composites of SCHL anomalies, surface NO_3, and surface PO_4 anomalies during

167   the decaying summer season following the mature phase of El Niño from all El-Niño cases in the GFDL-CM2.1

168   ESM model over a total period of 1,000 years. Unlike the satellite-observed SCHL anomalies shown in Fig. 1a

169   which are concentrated in the YRE region and gradually weakened outwards, the model results depict a diagonal

170 band pattern extending from the southeastern part of China to the Korean Strait (Figure 3a). This anomalous SCHL

171 pattern is somewhat consistent with the weak rightward diagonal pattern shown in Fig. 1a. Surface NO_3 anomalies

172 in Fig. 3b exhibit strong signals primarily in the YRE region, akin to the SCHL anomalies observed in Fig. 1a.

173 This similarity can be attributed to the ESM's incorporation of N inputs from riverine runoff, effectively capturing

174 the observed patterns. In contrast, surface PO_4 anomalies (Figure 3c) show a diagonal shape with a positive signal

175 from the northeastern part of Taiwan to the Korean strait. Given that the ESM does not include P input from

176 riverine sources, this anomalous PO_4 pattern can be driven by alternative processes. Therefore, it is essential to

177 explore additional mechanisms for phytoplankton blooming beyond the runoff-driven mechanisms.
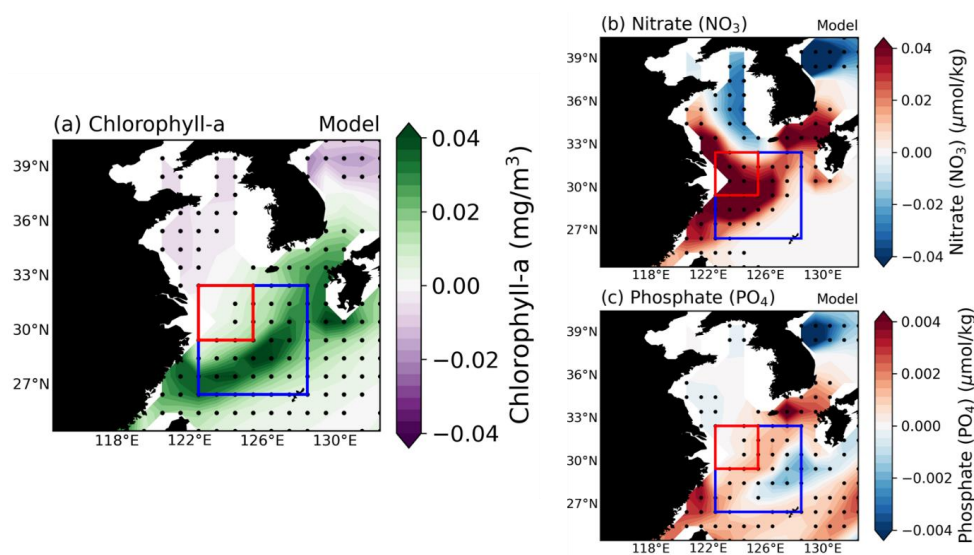
179 **Figure 3. (a-c)** Composite maps illustrate the SCHL, surface NO_3, and surface PO_4 distribution of El Niño
180 decaying summer season over the East China Sea (ECS) for all El Niño cases (176 years) which were selected in
181 GFDL-CM2.1 ESM results. All the black dots indicate where the responses are statistically significant at the 95%
182 confidence level, determined using the bootstrap method.

184 We examined the relationship between the DJF Niño3.4 index and SCHL anomalies in the ECS region,

185 showing a significant positive correlation (r = 0.51**) at the 99% confidence level (Figure 4a). From the long-

186 term integrated ESM results, we identified a total of 176 El Niño cases. Most of these cases result in positive

187 anomalous SCHL blooming, however, about 25% of the total El Niño cases exhibit negative SCHL anomalies. To

188 identify the processes responsible for the differing blooming outcomes, we divided the El Niño cases into two

189 groups based on the magnitude of anomalous SCHL blooming in the target region. The Strong Blooming (SB)

190 group, comprising the top 30 cases exhibiting strong blooming colored in reds, and the Non-Blooming (NB) group,

191 comprising the bottom 30 cases colored in blues (Figure 4b).

192 The composite map of SCHL anomalies during the El Niño decaying summer of the SB group reveals

193 pronounced anomalous blooming across the ECS region, while the NB group is characterized by negative SCHL

194   anomalies (Figure 4b, Figs. S1a-c). Surface nutrient distributions from the composite maps also show contrasting

195   results between the two groups during the El Niño decaying summer (Figs. S1d-i). To investigate the runoff-driven

196   phytoplankton blooming mechanism, as discussed in previous studies and above, we analyzed the composite

197   patterns of precipitation and runoff anomalies during the El Niño decaying summer season by comparing the two

198   groups (Figure 5). In terms of precipitation patterns, the SB group exhibits a broad positive rainfall band extending

199   over the entire East Asia region, from central China to Japan. In contrast, the NB group shows only weak positive

200   precipitation anomalies, confined to a narrow region of China, Taiwan, and the southern part of Japan. Similarly,

201   the runoff anomaly patterns display positive signals centered on the YRE region and the northern part of the YRE

202   region for both groups, with significance observed only in the SB group. The NB group, however, exhibits only

203   weakly significant positive patterns around the southern part of the YRE region. Moreover, the relationship

204   between runoff anomalies and the SCHL anomalies in the target region demonstrates a significantly positive

205   correlation (r = 0.59**) at the 99% confidence level, indicating that the runoff-driven mechanism is well simulated

206   in the model (Figure 5g).

207
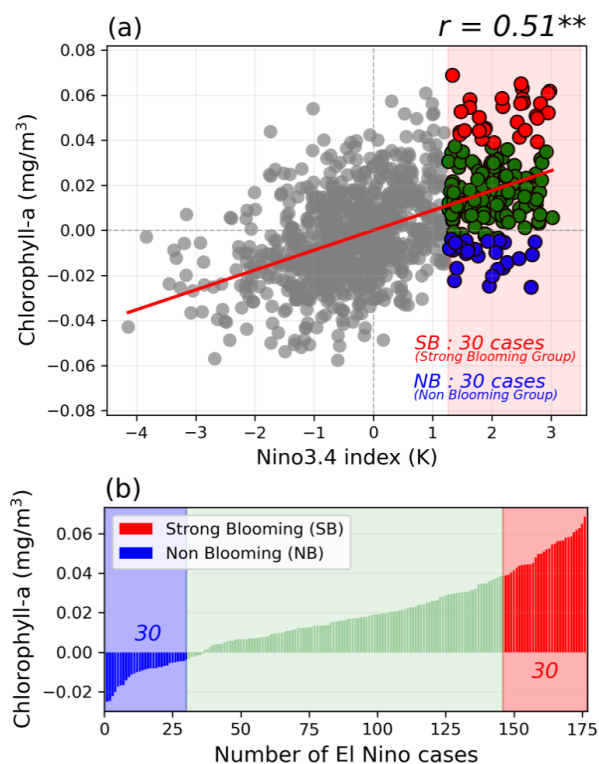
Figure 4. (a) The relationship between Niño3.4 DJF index and area-averaged SCHL anomalies over the target
region in GFDL-CM2.1 Earth System Model (ESM). **(b)** Categorization of all El Niño cases by the magnitude of
SCHL blooming in the target region of the ECS during El Niño decaying summers. The top 30 and bottom 30
cases, distinguished by SCHL anomaly magnitudes over the target region, colored in red and blue are grouped
into the Strong Blooming El Niño (SB) group and the Non-Blooming El Niño (NB) group, respectively.
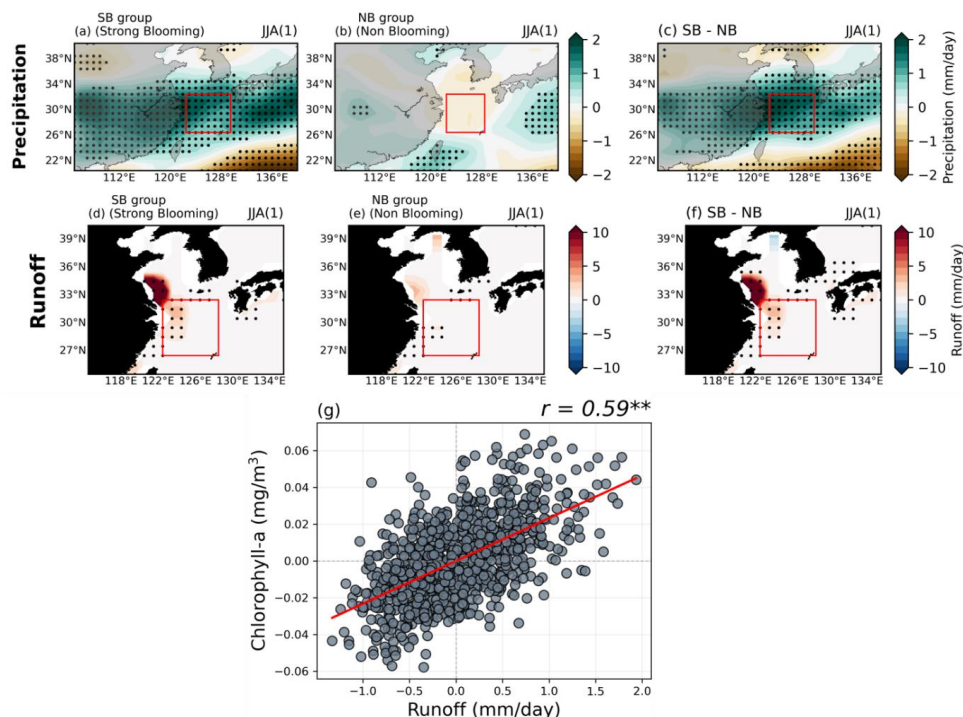
214 **Figure 5. (a-c)** Composite maps exhibiting precipitation anomalies during the El Niño decaying summer season
215 for both groups, as well as the difference between the two groups. **(d-f)** Similar to Figs. 5a-c, these maps
216 demonstrate a composite map of runoff anomalies during the El Niño decaying summer season for both groups,
217 as well as the difference between the two groups. **(g)** The relationship between area-averaged runoff and SCHL
218 anomalies over the target region.

219

**3.3. Upwelling-driven blooming mechanism - Insight from Model**

221   In addition to precipitation and runoff, there was a distinctive difference in the magnitude of upwelling

222 between the two groups. Figures 6a-b show the composite map of Ekman Upwelling (EKU) anomalies during the

223 El Niño decaying summer season. For the SB group, a significant positive EKU pattern dominates the ECS region,

224 with significantly negative EKU distribution in the WNP region, far south of Japan (Figure 6a). On the other hand,

225 the NB group does not exhibit any significant EKU anomaly patterns in the target region, with significant positive

226 EKU patterns over the southern part of Japan and negative EKU anomalies in the WNP but without significance

227 (Figure 6b). The difference between the two groups highlights distinct EKU anomaly patterns in the target region

228 (Figure 6c). The intensified EKU in the target region facilitates the transport of abundant nutrients from the

229 subsurface layer to the surface layer, thereby enhancing phytoplankton growth. This is supported by the

230 significantly positive correlation ($r = 0.47^{**}$) at the 99% confidence level between EKU anomalies and SCHL

231 anomalies in the target region, indicating that EKU can significantly contribute to anomalous phytoplankton

232 blooming, similar to the runoff-driven mechanism (Figure 6d).

233   EKU is primarily generated by cyclonic atmospheric circulations. The presence of robust upwelling in

234 the ECS region signifies the formation of cyclonic circulation, i.e. the EKU and wind stress curl (WSCL) are fully

235 positively correlated (Fig. S2a). During the El Niño mature phase, suppressed convection in the western Pacific

236 induces the Western North Pacific Anticyclone (WNPAC) in the lower-troposphere structure (Gill, 1980; Matsuno,

237 1966). Moreover, the WNPAC leads to cyclonic circulation in the northwestward ECS region via low-level Rossby

238 wave energy propagation (Wang et al., 2000). This sequence of wave patterns in the lower troposphere can

239 generate the WNPAC and atmospheric cyclonic circulation in the ECS region during the El Niño decaying summer

240 seasons. Given the significant differences in the magnitude and extent of rainfall band between the two groups,

241 we would expect distinct differences in the growth of WNPAC between the two groups as well. This suggests that

242 the differences in WNPAC development contribute to the variability in EKU and, consequently, the extent of

243 phytoplankton blooming in the ECS region during El Niño decaying summers.

244
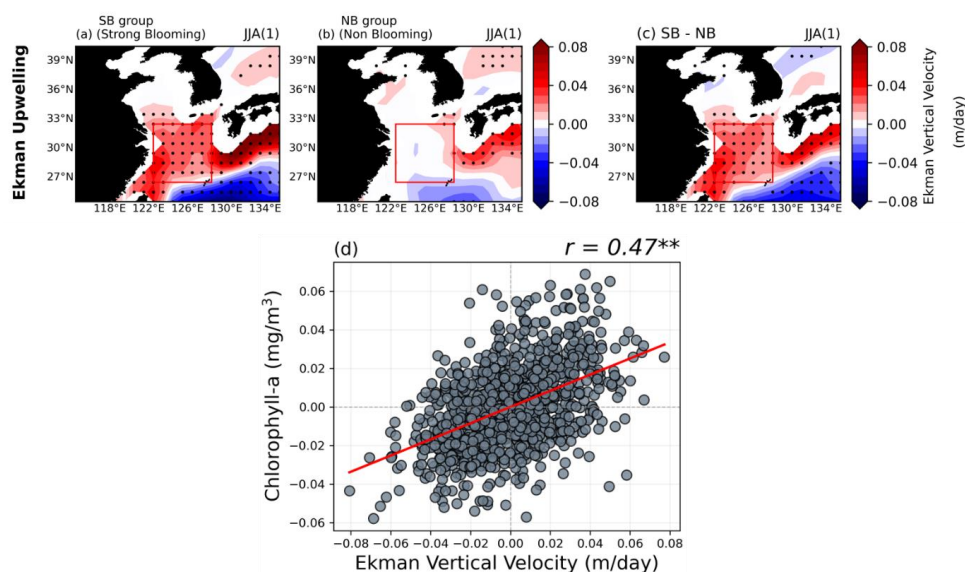
Figure 6. (a-c) Composite maps exhibiting Ekman Upwelling (EKU) anomalies during the El Niño decaying
246 summer season for both groups, as well as the difference between the two groups. **(d)** The relationship between
247 area-averaged EKU and SCHL anomalies over the target region.

248

249   Figure 7 illustrates the evolution of geopotential height (GPH) differences with 850hPa wind (Left

250 panels) and WSCL anomalies (Right panels) between two groups in the WNP across three seasons (D(0)JF(1)-

251 MAM(1)-JJA(1)) following El Niño mature phase. In the SB group, the WNPAC and North Pacific Cyclone (NPC)

252 are prominently stronger, positioned over the Philippines and North Pacific, respectively (Figure 7a). These

253 atmospheric circulations result in anomalous positive WSCL around the Korean Peninsula, Japan, and East Sea,

254 while negative WSCL is observed southeastern of China (Figure 7d). As the seasons progress, the WNPAC

255 migrates northeastward, becoming more pronounced in the SB group compared to the NB group, continuing into

256 the subsequent summer (Figures 7b-c). Positive WSCL anomalies begin to emerge in the ECS region from El

257 Niño decaying spring season, coinciding with the developed WNPAC (Figure 7e). By summer, the WNPAC in

258   the SB group is intensely and broadly developed, dominating the WNP, leading to a stronger cyclonic circulation

259   in the ECS region and enhanced wind-driven EKU due to positive WSCL (Figure 7c and Figure 7f). The

260   correlation between WSCL and the WNPAC index calculated from GPH anomalies within the red box in Fig. 7g

261   exhibits a significantly positive relationship (r = 0.45**) at the 99% confidence level. This implies that the

262   development of a stronger WNPAC may lead to the generation of anomalous positive WSCL, prompting

263   upwelling and facilitating anomalous phytoplankton blooming during El Niño decaying summers.

264

265
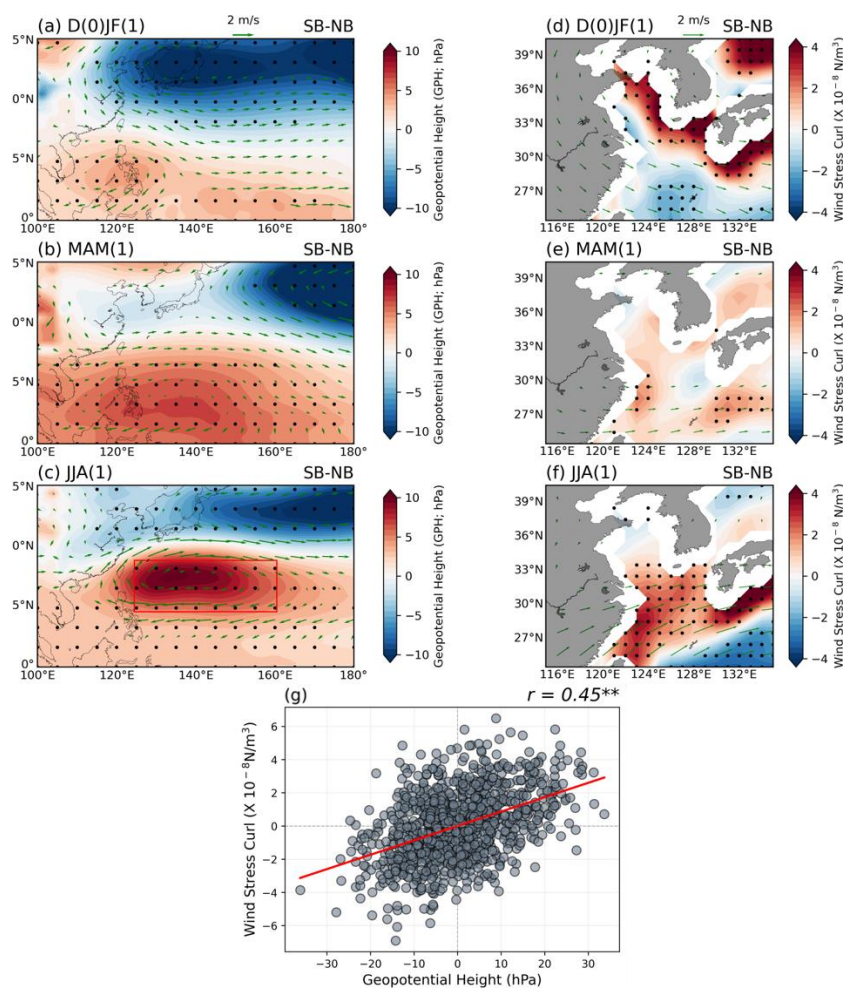
Figure 7. Evolution map of El Niño composite of **(a-c)** geopotential height (GPH; Left panels) and **(d-f)** Wind
Stress Curl (WSCL; Right panels) with 850hPa wind anomalies (vectors) from El Niño mature phase to decaying
summer season for the differences between two groups. **(g)** The relationship between area-averaged Western North
Pacific (WNP) GPH anomalies (highlighted as a red box in Fig. 7c) and Wind Stress Curl (WSCL) anomalies
over the target region. All the black dots indicate where the responses are statistically significant at the 95%
confidence level, determined using the bootstrap method.

272   As shown in Fig. 5 and Fig. 6, both the runoff-driven and upwelling-driven mechanisms work to
273 contribute to the strong blooming observed in the SB group. To quantify the relative contributions of these
274 mechanisms, we applied partial correlation and joint composite analyses. The partial correlation analysis revealed
275 that the impact of the runoff-driven mechanism on phytoplankton blooming, after removing the effect of the
276 upwelling-driven mechanism, is 0.49**. Conversely, the effect of the upwelling-driven mechanism on
277 phytoplankton blooming, after accounting for the runoff-driven mechanism, is 0.31**. These results indicate that
278 while both mechanisms play significant roles, the runoff-driven mechanism has a relatively stronger influence.

279   Additionally, the joint composite analysis further demonstrated that both mechanisms contribute to
280 anomalous phytoplankton blooming. We performed this analysis by assessing the relative strengths of runoff and
281 WSCL in the target region (Figure 8a). We categorized the 176 El Niño cases into four groups based on whether
282 the runoff and WSCL anomalies were positive or negative during the decaying summer season of El Niño events
283 (Figure 8b). The results showed that 62% (109 cases) of the El Niño cases exhibited both positive runoff and
284 WSCL anomalies. Furthermore, 13% (22 cases) and 11% (19 cases) displayed positive anomalies for either WSCL
285 or runoff, respectively, while 15% (26 cases) were negative for both. The magnitude of anomalous blooming was
286 highest when both WSCL and runoff anomalies were positive. The average blooming magnitude when WSCL
287 was positive but runoff anomalies were negative was almost the same, with little weakness of about 8% (0.0007
288 mg m^{-3}) compared to vice versa. When both were negative, the blooming magnitude was negative on average.
289 Importantly, a statistically significant positive blooming magnitude was observed only when both mechanisms
290 were positively contributing. Therefore, the combined effect of both mechanisms is crucial for the anomalous
291 phytoplankton blooming observed in the ECS region during the El Niño decaying summers.

292

293
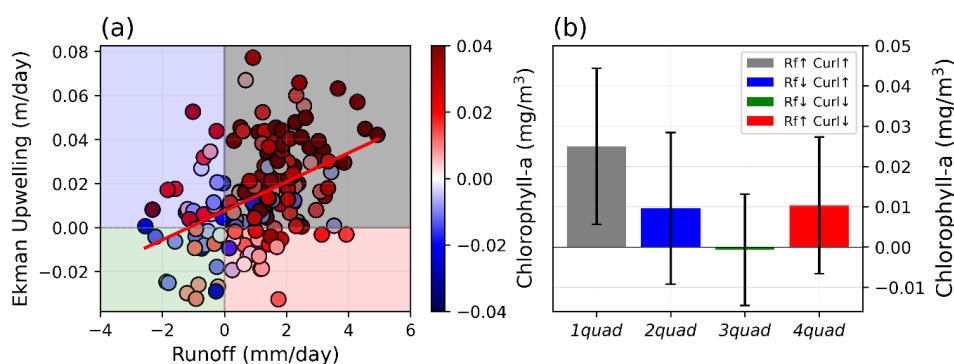
Figure 8. (a) The scatter plot indicates the runoff and wind stress curl in the target region during the following
summer season of all El Niño cases selected from the GFDL-CM2.1 ESM. Colored scatters show the anomalous
blooming magnitude in the target region. **(b)** Bar plots indicate the averaged anomalous blooming magnitude of
the selected El Niño cases of each quadrant in Fig. 8a over the target region. Crosses indicate the range of ±1
standard deviation.

299

300

### 3.4. Upwelling-driven blooming mechanism - Insight from Observations

So far, we have re-evaluated the runoff-driven mechanism using model results and identified an upwelling-driven mechanism. Lastly, we examined the upwelling-driven mechanism using reanalysis data for physical variables and chlorophyll-a satellite data to verify its application to the real world. Figure 9a shows the composite map of GPH anomalies during the El Niño decaying summer, using NCEP2 re-analysis data. To identify the typical WNPAC and 850hPa wind anomalies during El Niño decaying summers, we defined a WNPAC index using the full period of available NCEP2 re-analysis data (1979-2022; 44 years). The WNPAC index was defined as the area-averaged (16.5°N-26.5°N, 130°E-155°E) GPH anomalies over the WNP region indicated by the red box in Fig. 9a. The WNPAC pattern and anticyclonic 850hPa wind anomalies ranging from the South China Sea to the WNP, are well represented in the re-analysis data. We calculated the WSCL using surface winds from the NCEP2 re-analysis data, revealing significant positive WSCL (cyclonic circulation) anomalies over a large area of southeastern China (Figure 9b). Furthermore, we found a significant positive correlation ($r = 0.56^{**}$) at the 99% confidence level between the WSCL index (red box in Fig. 9b) and SCHL anomalies in the target region (Figure 9c). Additionally, there is a significant positive correlation ($r = 0.43^{*}$) at the 95% confidence level between the WNPAC index and the SCHL anomalies in the target region (Figure 9d). A strong positive relationship ($r = 0.56^{**}$) at the 99% confidence level between the WNPAC index and WSCL in the target region was also observed (Figure 9e). Several instances of negative SCHL anomalies occurred despite positive anomalous rainfall (blue box in Fig. 9a; 28.5°N-33.5°N, 111°E-120°E). However, interestingly, cases exhibiting strong anomalous SCHL blooming mostly coincided with either strong WNPAC indices or robust cyclonic WSCL in the ECS region (Figure 9e). These remarkable associations among these variables suggest that the upwelling-driven blooming mechanism is indeed operating in the real world. Therefore, both the runoff-driven and upwelling-driven mechanisms must be considered together to fully understand the dynamics of phytoplankton blooming in the ECS region during El Niño decaying summers.
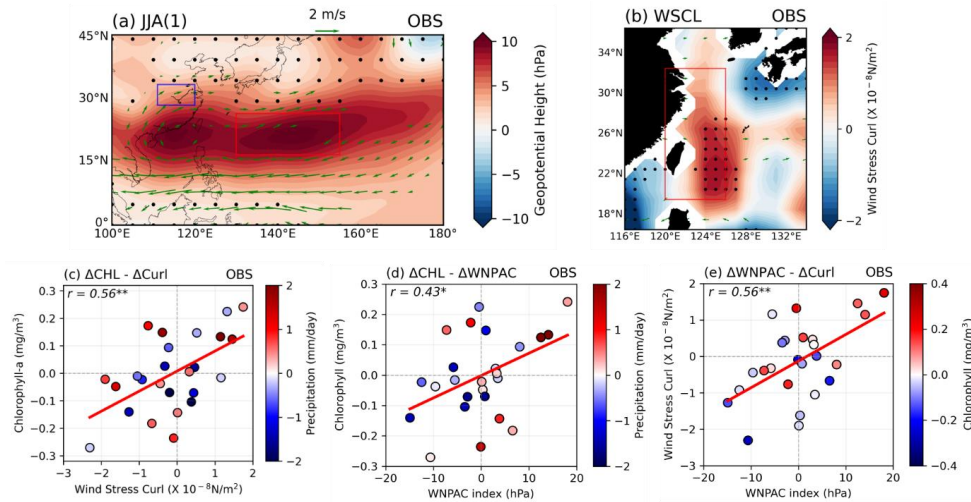
Figure 9. (a) The composite map exhibits the GPH anomalies over the WNP and 850hPa wind anomaly patterns during the El Niño decaying summer season for the available period of re-analysis data (1979-2022; 44 years). Red and blue boxes indicate the area-averaged WNPAC index (16.5°N-26.5°N, 130°E-155°E) and precipitation index (28.5°N- 33.5°N, 111°E-120°E) respectively. Black dots indicate the insignificance at the 90% confidence level using the bootstrap method. **(b)** The composite map shows WSCL anomaly patterns and 850hPa wind anomaly patterns during the El Niño decaying summer season within the same period with Fig. 9a. The red box indicates the area-averaged WSCL index. Black dots indicate the significance at the 90% confidence level using the bootstrap method. **(c-d)** The relationship between SCHL anomalies in the target region and the WSCL index and the WNPAC index respectively. Colored scatters show the precipitation index over the eastern part of China. **(e)** The relationship between the WNPAC index and the WSCL index. Colored scatters show the magnitude of SCHL anomalies in the target region.

4. Discussions

This study investigates the comprehensive mechanisms of anomalous phytoplankton blooms in the East China Sea during the summer following El Niño events. We re-evaluated the existing runoff-driven phytoplankton blooming mechanism using the observational data and long-term integrated ESM results based on present climate conditions. Notably, the ESM we used does not simulate P riverine input, a crucial factor in the YRE region, our research target region. Despite the absence of P riverine inputs, significant positive phytoplankton blooms still emerged, we hence proposed an additional mechanism to trigger anomalous phytoplankton blooming during the summers following the El Niño mature phase.

Firstly, we sorted all El Niño cases selected from long-term climate simulation results based on the magnitude of SCHL blooming in the ECS region and classified the El Niño cases into two groups (SB & NB group). There were clear differences between the two groups in climatic factors such as precipitation and runoff, which drive existing blooming mechanisms. In the SB group, stronger and broader rainfall band and riverine inputs into the ECS region were significantly predominant. The rainfall band generated over East Asia during the summer season of post-El Niño is related to the development of the WNPAC, suggesting that the WNPAC is more potently advanced in the SB group.

In addition, distinct differences between the two groups were observed, evident in both the magnitude of EKU anomalies induced by atmospheric circulation and the WSCL anomaly patterns. Consequently, We found a more robust and expansive WNPAC that persisted and extended its influence until the summer season, impacting a broader area of East Asia in the SB group. This well-developed WNPAC triggers stronger wind anomalies in the target region, leading to active EKU with positive WSCL. It facilitates upwelling in the water column as the cyclonic atmospheric circulation, driven by the strong clockwise circulation over WNP, prevailed across the entire ECS region.

Lastly, we validated the upwelling-driven phytoplankton blooming mechanism elucidated by the model results using reanalysis data and satellite chlorophyll-a data. There was a significantly positive relationship between WNPAC and SCHL anomalies, as well as WNPAC and WSCL anomalies in the target region. Thus, depending on the development of WNPAC during the El Niño decaying summers, anomalous phytoplankton blooms can be triggered by a conjunction of different mechanisms: runoff-driven accompanied by strong precipitation in the ECS region, as well as upwelling-driven mechanism induced by positive WSCL and EKU.

We investigated that the more vigorous development and expansion of the WNPAC can influence the marine ecosystems of the ECS region with sufficient El Niño cases using ESM results. The intensity and extent of WNPAC development between the SB and NB groups were distinct, which means that anomalous phytoplankton blooming can be predicted as early as two seasons before it occurs during the El Niño mature phase. We found a significantly positive lagged relationship between the WNPAC index and blooming magnitude in the ECS region in both observations and ESM results (Figure 10). There were significant 2 seasons (D(0)JF(1) – JJA(1)) lagged positive correlations (r = 0.61**) and ESM results (r = 0.5**). In addition, the case of a short-term, 1 season lagged relationship (MAM(1) – JJA(1)) has higher lagged positive correlations in both observations (r = 0.69**) and ESM results (0.57**) at the 99% confidence level. These results demonstrate that the magnitude of

374   WNPAC during the El Niño mature phase can be a good predictor of the magnitude of phytoplankton blooms in
375   the ECS region during the following summers of El Niño events.

376   The present climate-based long-term integrated ESM (GFDL-CM2.1) utilized in this study, possesses a
377   relatively low spatial resolution, leading to coarse representations of features like continental shelves and slopes
378   like those in the YECS region. This limitation may hinder the accurate depiction of regional currents and local
379   eddies, which are crucial for understanding ocean circulation dynamics, including the intrusion of the Kuroshio
380   current near the north-eastern part of Taiwan Island, as mentioned in previous studies (Chen, 1996; Chen et al.,
381   1995; Lee et al., 2023). However, since we are arguing for an upwelling mechanism in the ocean driven by
382   atmospheric circulation rather than horizontal transport, the resolution limitation may not significantly impact our
383   findings. Furthermore, our analyses are based on the present climate-based long-term integrated ESM, and there
384   may be changes in the pattern of WNPAC development due to changes in the ENSO teleconnection resulting from
385   changes in the El Niño mean state under global warming scenarios (Kim et al., 2024; Shin et al., 2022; Yang et
386   al., 2022; Yeh et al., 2009). Here, we primarily focused on the biological aspect of the phytoplankton blooming
387   mechanism and did not extensively explore the dynamic mechanisms driving differences in WNPAC development
388   intensity between the two groups. In Fig. S3, we identified differences in the decaying speed of the El Niño
389   strength between the two groups and the warmer SST anomalies in the Central Pacific (CP) region during El Niño
390   mature phase in the SB group. Therefore, further studies will be necessary to investigate the blooming magnitude
391   variations associated with different El Niño types such as CP and Eastern Pacific (EP) El Niño (Kug et al., 2009,
392   2010; Yuan and Yang, 2012). Moreover, Xie et al mentioned that the anomalous large-scale anti-cyclone in the
393   WNP during the summer season of the El Niño decaying is associated with the Indian Ocean (IO), named the IO
394   Capacitor theory. These dynamic aspects will require further detailed exploration in subsequent studies.
395   Additionally, quantitative analyses between runoff-driven and upwelling-driven blooming mechanisms through
396   model experiments will be necessary to provide a detailed understanding of the contribution of both mechanisms
397   to phytoplankton blooms during the El Niño decaying summer season.
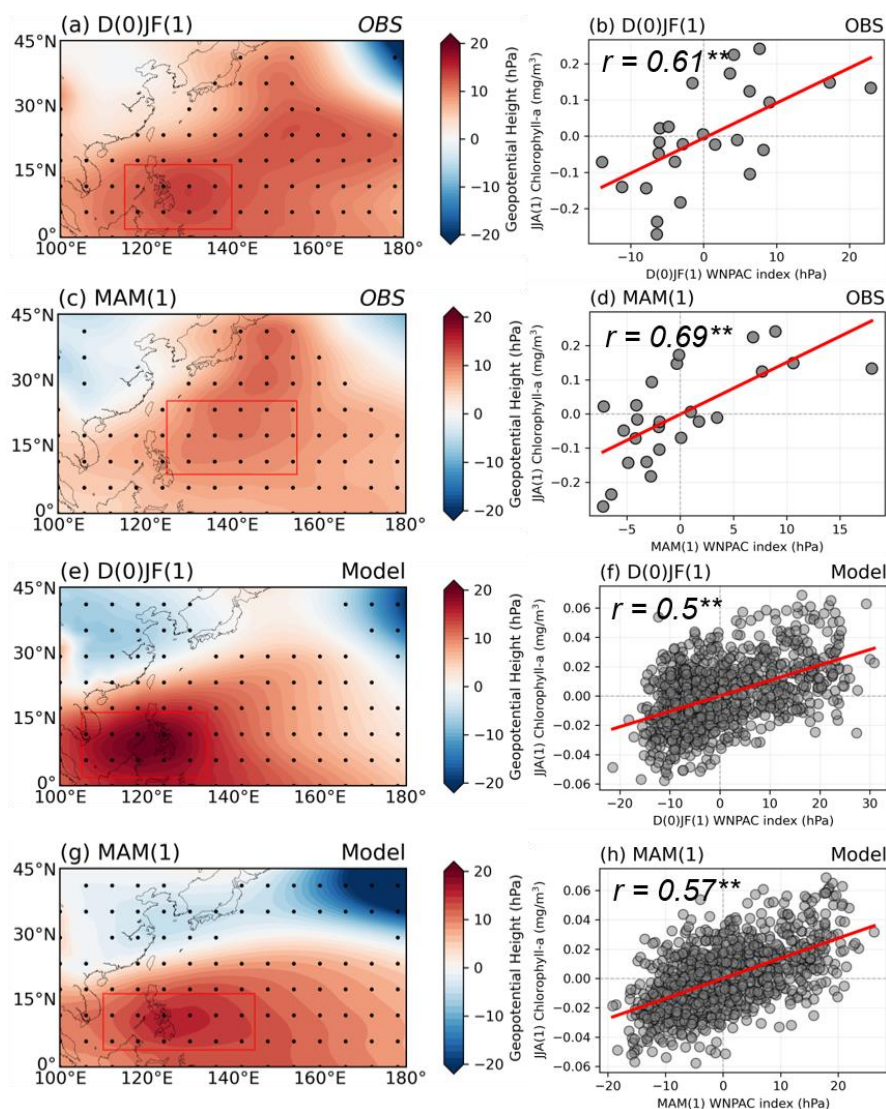
Figure 10. (a-d) Evolution maps indicate the distribution of GPH anomalies from the mature phase (D(0)JF(1)) of El Niño to the following spring season (MAM(1)) in the observations. Scatter plots show the lagged relationship between the area-averaged WNPAC index (red box in the left panels) during each period and the anomalous SCHL blooming magnitude in the target region during the decaying summers of the El Niño in observations. **(e-h)** Same as (a-d), but with model results.

Data availability

The chlorophyll satellite observation data used in this study is available on https://esa-oceancolour-cci.org. The ERSST (SST), wind, wind stress, GPH re-analysis data are provided at https://psl.noaa.gov/.

Code availability

The computer codes that support the analysis within this paper are available from the corresponding author on request.

Funding

This work was sponsored by a research grant from the National Research Foundation of Korea (NRF-2021M3I6A1086808), and supported by Research of Long-term Marine Environmental Change in the Yellow Sea and East China Sea Using the Ieodo Ocean Research Station (Ieodo-ORS) form the Korean Hydrographic and Oceanographic Agency (KHOA).

Ethical approval

Not applicable

Declaration of Competing interests

The authors declare no competing interests.

CrediT authorship contribution statement

425

426 **Dong-Geon Lee:** compiled the data, conducted analyses, prepared the figures, and wrote the

427 manuscript. **Jong-Seong Kug:** Designed the research and wrote the majority of the manuscript

428 content. All the authors discussed the study results and reviewed the manuscript.

References

Beardsley, R. C., Limeburner, R., Yu, H., and Cannon, G. A.: Discharge of the Changjiang (Yangtze River) into the East China Sea, Cont. Shelf Res., 4, 57–76, https://doi.org/10.1016/0278-4343(85)90022-6, 1985.

Behrenfeld, M. J., O'Malley, R. T., Siegel, D. A., McClain, C. R., Sarmiento, J. L., Feldman, G. C., Milligan, A. J., Falkowski, P. G., Letelier, R. M., and Boss, E. S.: Climate-driven trends in contemporary ocean productivity, Nature, 444, 752–755, https://doi.org/10.1038/nature05317, 2006.

Cavcar, M.: International Standard Atmosphere, in BS, Anadolu Univ., 30(9), 1–6, 2000.

Chen, C.-T. A.: The Kuroshio intermediate water is the major source of nutrients on the East China Sea continental shelf, Oceanol. Acta, 19, 523–527, 1996.

Chen, C. T. A., Ruo, R., Paid, S. C., Liu, C. T., and Wong, G. T. F.: Exchange of water masses between the East China Sea and the Kuroshio off northeastern Taiwan, Cont. Shelf Res., 15, 19–39, https://doi.org/10.1016/0278-4343(93)E0001-O, 1995.

Danielsdottir, M. G., Brett, M. T., and Arhonditsis, G. B.: Phytoplankton food quality control of planktonic food web processes, Hydrobiologia, 589, 29–41, https://doi.org/10.1007/s10750-007-0714-6, 2007.

Dunne, J., Gnanadesikan, A., Sarmiento, J. L., and Slater, R. D.: Technical description of the prototype version (v0) of Tracers Of Phytoplankton with Allometric Zooplankton (TOPAZ) ocean biogeochemical model as used in the Princeton IFMIP* model, Biogeosciences, 7, 3593, 2010.

Dunne, J. P., John, J. G., Shevliakova, E., Stouffer, R. J., Krasting, J. P., Malyshev, S. L., Milly, P. C. D., Sentman, L. T., Adcroft, A. J., Cooke, W., Dunne, K. A., Griffies, S. M., Hallberg, R. W., Harrison, M. J., Levy, H., Wittenberg, A. T., Phillips, P. J., and Zadeh, N.: GFDL's ESM2 Global Coupled Climate–Carbon Earth System Models. Part II: Carbon System Formulation and Baseline Simulation Characteristics*, J. Clim., 26, 2247–2267, https://doi.org/10.1175/JCLI-D-12-00150.1, 2013.

Field, C. B., Behrenfeld, M. J., Randerson, J. T., and Falkowski, P.: Primary production of the biosphere: Integrating terrestrial and oceanic components, Science (80-.)., 281, 237–240,

458   https://doi.org/10.1126/science.281.5374.237, 1998.

459   Gill, A. E.: Some simple solutions for heat-induced tropical circulation, Q. J. R. Meteorol. Soc.,

460   106, 447–462, https://doi.org/10.1002/qj.49710644905, 1980.

461   He, X., Bai, Y., Pan, D., Chen, C. T. A., Cheng, Q., Wang, D., and Gong, F.: Satellite views of

462   the seasonal and interannual variability of phytoplankton blooms in the eastern China seas over

463   the past 14 yr (1998-2011), Biogeosciences, 10, 4721–4739, https://doi.org/10.5194/bg-10-

464   4721-2013, 2013.

465   Henson, S. A., Sarmiento, J. L., Dunne, J. P., Bopp, L., Lima, I., Doney, S. C., John, J., and

466   Beaulieu, C.: Detection of anthropogenic climate change in satellite records of ocean

467   chlorophyll and productivity, Biogeosciences, 7, 621–640, https://doi.org/10.5194/bg-7-621-

468   2010, 2010.

469   Huang, B., Thorne, P. W., Banzon, V. F., Boyer, T., Chepurin, G., Lawrimore, J. H., Menne,

470   M. J., Smith, T. M., Vose, R. S., and Zhang, H. M.: Extended reconstructed Sea surface

471   temperature, Version 5 (ERSSTv5): Upgrades, validations, and intercomparisons, J. Clim., 30,

472   8179–8205, https://doi.org/10.1175/JCLI-D-16-0836.1, 2017.

473   Huang, T. H., Chen, C. T. A., Lee, J., Wu, C. R., Wang, Y. L., Bai, Y., He, X., Wang, S. L.,

474   Kandasamy, S., Lou, J. Y., Tsuang, B. J., Chen, H. W., Tseng, R. S., and Yang, Y. J.: East

475   China Sea increasingly gains limiting nutrient P from South China Sea, Sci. Rep., 9, 1–10,

476   https://doi.org/10.1038/s41598-019-42020-4, 2019.

477   Kanamitsu, M., Wesley, E., Jack, W., Yang, S., Hnilo, J. J., Fiorino, M., and Potter, G. L.:

478   NCEP–DOE AMIP-II Reanalysis (R-2), Bull. Am. Meteorol. Soc., 83, 1631–1644,

479   https://doi.org/10.1175/BAMS-83-11-1631, 2002.

480   Kessler, W. S.: The circulation of the eastern tropical Pacific: A review, Prog. Oceanogr., 69,

481   181–217, https://doi.org/10.1016/j.pocean.2006.03.009, 2006.

482   Kim, G. Il, Oh, J. H., Shin, N. Y., An, S. Il, Yeh, S. W., Shin, J., and Kug, J. S.: Deep ocean

483   warming-induced El Niño changes, Nat. Commun., 15, 1–8, https://doi.org/10.1038/s41467-

484   024-50663-9, 2024.

485   Kim, S. and Kug, J. S.: What Controls ENSO Teleconnection to East Asia? Role of Western

486   North Pacific Precipitation in ENSO Teleconnection to East Asia, J. Geophys. Res. Atmos.,

487   123, 10,406-10,422, https://doi.org/10.1029/2018JD028935, 2018.

488   Kim, T.-W., Lee*, K., Najja Raymond G, Jeong, H.-D., and Jeong, H. J.: Increasing N
489   Abundance in the Northwestern Pacific Ocean Due to Atmospheric Nitrogen Deposition,
490   Science (80-.)., 334, 505–509, https://doi.org/DOI: 10.1126/science.1206583, 2011.

491   Kug, J.-S., Jin, F.-F., and An, S.-I.: Two Types of El Niño Events: Cold Tongue El Niño and
492   Warm Pool El Niño, J. Clim., 22, 1499–1515, https://doi.org/10.1175/2008JCLI2624.1, 2009.

493   Kug, J. S., Choi, J., An, S. Il, Jin, F. F., and wittenberg, A. T.: Warm pool and cold tongue El
494   Niño events as simulated by the GFDL 2.1 coupled GCM, J. Clim., 23, 1226–1239,
495   https://doi.org/10.1175/2009JCLI3293.1, 2010.

496   Kwon, M. H., Jhun, J. G., Wang, B., An, S. Il, and Kug, J. S.: Decadal change in relationship
497   between east Asian and WNP summer monsoons, Geophys. Res. Lett., 32, 1–4,
498   https://doi.org/10.1029/2005GL023026, 2005.

499   Lee, D. G., Oh, J. H., Noh, K. M., Kwon, E. Y., Kim, Y. H., and Kug, J. S.: What controls the
500   future phytoplankton change over the Yellow and East China Seas under global warming?,
501   Front. Mar. Sci., 10, 1–9, https://doi.org/10.3389/fmars.2023.1010341, 2023.

502   Li, T., Wang, B., Wu, B., Zhou, T., Chang, C.-P., and Zhang, R.: Theories on formation of an
503   anomalous anticyclone in western North Pacific during El Niño: A review, J. Meteorol. Res.,
504   31, 987–1006, https://doi.org/10.1007/s13351-017-7147-6, 2017.

505   Li, T., Wang, B., and Chang, C. P.: A review of mechanisms for formation of an anomalous
506   anticyclone in western north pacific during el niño, Multiscale Glob. Monsoon Syst., 31, 91–
507   102, https://doi.org/10.1142/9789811216602_0008, 2021.

508   Liu, K. K., Chao, S. Y., Lee, H. J., Gong, G. C., and Teng, Y. C.: Seasonal variation of primary
509   productivity in the East China Sea: A numerical study based on coupled physical-
510   biogeochemical model, Deep. Res. Part II Top. Stud. Oceanogr., 57, 1762–1782,
511   https://doi.org/10.1016/j.dsr2.2010.04.003, 2010.

512   Liu, S. M., Zhang, J., and Jiang, W. S.: Pore water nutrient regeneration in shallow coastal
513   Bohai Sea, China, J. Oceanogr., 59, 377–385, https://doi.org/10.1023/A:1025576212927, 2003.

514   Matsuno, T.: Quasi-Geostrophic Motions in the Equatorial Area, J. Meteorol. Soc. Japan. Ser.
515   II, 44, 25–43, https://doi.org/10.2151/jmsj1965.44.1_25, 1966.

516 Moon, J. Y., Lee, K., Lim, W. A., Lee, E., Dai, M., Choi, Y. H., Han, I. S., Shin, K., Kim, J.
517 M., and Chae, J.: Anthropogenic nitrogen is changing the East China and Yellow seas from
518 being N deficient to being P deficient, Limnol. Oceanogr., 66, 914–924,
519 https://doi.org/10.1002/lno.11651, 2021.

520 Park, T., Jang, C. J., Kwon, M., Na, H., and Kim, K. Y.: An effect of ENSO on summer surface
521 salinity in the Yellow and East China Seas, J. Mar. Syst., 141, 122–127,
522 https://doi.org/10.1016/j.jmarsys.2014.03.017, 2015.

523 Racault, M. F., Sathyendranath, S., Brewin, R. J. W., Raitsos, D. E., Jackson, T., and Platt, T.:
524 Impact of El Niño variability on oceanic phytoplankton, Front. Mar. Sci., 4, 133,
525 https://doi.org/10.3389/fmars.2017.00133, 2017.

526 Sathyendranath, S., Brewin, R. J. W., Brockmann, C., Brotas, V., Calton, B., Chuprin, A.,
527 Cipollini, P., Couto, A. B., Dingle, J., Doerffer, R., Donlon, C., Dowell, M., Farman, A., Grant,
528 M., Groom, S., Horseman, A., Jackson, T., Krasemann, H., Lavender, S., Martinez-Vicente,
529 V., Mazeran, C., Mélin, F., Moore, T. S., Müller, D., Regner, P., Roy, S., Steele, C. J.,
530 Steinmetz, F., Swinton, J., Taberner, M., Thompson, A., Valente, A., Zühlke, M., Brando, V.
531 E., Feng, H., Feldman, G., Franz, B. A., Frouin, R., Gould, R. W., Hooker, S. B., Kahru, M.,
532 Kratzer, S., Mitchell, B. G., Muller-Karger, F. E., Sosik, H. M., Voss, K. J., Werdell, J., and
533 Platt, T.: An ocean-colour time series for use in climate studies: The experience of the ocean-
534 colour climate change initiative (OC-CCI), Sensors (Switzerland), 19,
535 https://doi.org/10.3390/s19194285, 2019.

536 Shi, W. and Wang, M.: Satellite views of the Bohai Sea, Yellow Sea, and East China Sea, Prog.
537 Oceanogr., 104, 30–45, https://doi.org/10.1016/j.pocean.2012.05.001, 2012.

538 Shin, N. Y., Kug, J. S., Stuecker, M. F., Jin, F. F., Timmermann, A., and Kim, G. Il: More
539 frequent central Pacific El Niño and stronger eastern pacific El Niño in a warmer climate, npj
540 Clim. Atmos. Sci., 5, 1–8, https://doi.org/10.1038/s41612-022-00324-9, 2022.

541 Son, H. Y., Park, J. Y., Kug, J. S., Yoo, J., and Kim, C. H.: Winter precipitation variability
542 over Korean Peninsula associated with ENSO, Clim. Dyn., 42, 3171–3186,
543 https://doi.org/10.1007/s00382-013-2008-1, 2014.

544 Tong, Y., Zhao, Y., Zhen, G., Chi, J., Liu, X., Lu, Y., Wang, X., Yao, R., Chen, J., and Zhang,
545 W.: Nutrient Loads Flowing into Coastal Waters from the Main Rivers of China (2006-2012),

546   Sci. Rep., 5, 1–12, https://doi.org/10.1038/srep16678, 2015.

547   Trenberth, K. E., Large, W. G., and Olson, J. G.: The Mean Annual Cycle in Global Ocean

548   Wind Stress, J. Phys. Oceanogr., 20, 1742–1760, https://doi.org/10.1175/1520-

549   0485(1990)020<1742:TMACIG>2.0.CO;2, 1990.

550   Wang, B., Wu, R., and Fu, X.: Pacific-East Asian teleconnection: How does ENSO affect East

551   Asian climate?, J. Clim., 13, 1517–1536, https://doi.org/10.1175/1520-

552   0442(2000)013<1517:PEATHD>2.0.CO;2, 2000.

553   Wang, B., Wang, X., and Zhan, R.: Nutrient conditions in the Yellow Sea and the East China

554   Sea, Estuar. Coast. Shelf Sci., 58, 127–136, https://doi.org/10.1016/S0272-7714(03)00067-2,

555   2003.

556   Wu, Q., Wang, X., He, Y., and Zheng, J.: The Relationship between Chlorophyll Concentration

557   and ENSO Events and Possible Mechanisms off the Changjiang River Estuary, Remote Sens.,

558   15, https://doi.org/10.3390/rs15092384, 2023.

559   Wyrtki, K. and Meyers, G.: The Trade Wind Field Over the Pacific Ocean, J. Appl. Meteorol.,

560   15, 698–704, https://doi.org/10.1175/1520-0450(1976)015<0698:TTWFOT>2.0.CO;2, 1976.

561   Xie, S. P., Hu, K., Hafner, J., Tokinaga, H., Du, Y., Huang, G., and Sampe, T.: Indian Ocean

562   capacitor effect on Indo-Western pacific climate during the summer following El Niño, J. Clim.,

563   22, 730–747, https://doi.org/10.1175/2008JCLI2544.1, 2009.

564   Yamaguchi, H., Kim, H. C., Son, Y. B., Kim, S. W., Okamura, K., Kiyomoto, Y., and Ishizaka,

565   J.: Seasonal and summer interannual variations of SeaWiFS chlorophyll a in the Yellow Sea

566   and East China Sea, Prog. Oceanogr., 105, 22–29,

567   https://doi.org/10.1016/j.pocean.2012.04.004, 2012.

568   Yang, K., Cai, W., Huang, G., Hu, K., Ng, B., and Wang, G.: Increased variability of the

569   western Pacific subtropical high under greenhouse warming, Proc. Natl. Acad. Sci. U. S. A.,

570   119, 1–9, https://doi.org/10.1073/pnas.2120335119, 2022.

571   Yeh, S. W., Kug, J. S., Dewitte, B., Kwon, M. H., Kirtman, B. P., and Jin, F. F.: El Nĩo in a

572   changing climate, Nature, 461, 511–514, https://doi.org/10.1038/nature08316, 2009.

573   Yuan, Y. and Yang, S.: Impacts of different types of El NiñO on the East Asian climate: Focus

574   on ENSO cycles, J. Clim., 25, 7702–7722, https://doi.org/10.1175/JCLI-D-11-00576.1, 2012.

575   Zhai, F., Liu, Z., Gu, Y., He, S., Hao, Q., and Li, P.: Satellite-Observed Interannual Variations

576   in Sea Surface Chlorophyll-a Concentration in the Yellow Sea Over the Past Two Decades, J.

577   Geophys. Res. Ocean., 128, 1–23, https://doi.org/10.1029/2022JC019528, 2023.

578   Zhang, J.: Nutrient elements in large Chinese estuaries, Cont. Shelf Res., 16, 1023–1045,

579   https://doi.org/10.1016/0278-4343(95)00055-0, 1996.

580   Zhang, J., Liu, S. M., Ren, J. L., Wu, Y., and Zhang, G. L.: Nutrient gradients from the

581   eutrophic Changjiang (Yangtze River) Estuary to the oligotrophic Kuroshio waters and re-

582   evaluation of budgets for the East China Sea Shelf, Prog. Oceanogr., 74, 449–478,

583   https://doi.org/10.1016/j.pocean.2007.04.019, 2007.

584   Zhang, Y., Yu, Q., Ma, W., and Chen, L.: Atmospheric deposition of inorganic nitrogen to the

585   eastern China seas and its implications to marine biogeochemistry, J. Geophys. Res. Atmos.,

586   115, 1–10, https://doi.org/10.1029/2009JD012814, 2010.

587   Zhao, L. and Guo, X.: Influence of cross-shelf water transport on nutrients and phytoplankton

588   in the East China Sea: A model study, Ocean Sci., 7, 27–43, https://doi.org/10.5194/os-7-27-

589   2011, 2011.

590